Article

Extremely poleward shift of Antarctic Circumpolar Current by eccentricity during the Last Interglacial

Lijuan Lu [1,2,3,4], Xufeng Zheng [2] ✉, Michael E. Weber [5], Victoria Peck[6], Brendan T. Reilly[7], Zhong Chen[1,8], Wen Yan[1,8], Tianyu Chen [9], Hong Yan [10], Xun Gong [11,12], Shuzhuang Wu [13,14], Liwei Zheng[2], Shiming Wan [15], Yan Du [1], Lisa Tauxe [6], Qinghua Yang [3,4], Stefanie Brachfeld [16], Trevor Williams [17], Yasmina M. Martos [18,19], Zhiheng Du[20], Marga Garcia [21], Lara F. Pérez [22], Hu Yang [23], Bingyue Huang[2], Jonathan Warnock [24] & Shuh-Ji Kao[2] ✉

The Antarctic Circumpolar Current (ACC) exerts substantial control on the physical, chemical, and biological properties of the Southern Ocean, playing a key role in modulating the global carbon cycle and climate. However, the orbital-scale forcing and future changes in the strength and position of the ACC remain elusive. Here, we reconstruct the history of ACC extending back to the Last Interglacial (LIG; 128-113 ka) using sediment cores from the Scotia Sea. Based on high-resolution measurements of sortable silt mean grain size, we find that bottom current speed is synchronized with eccentricity, superimposed by precession. During the LIG when both eccentricity and precession reached their maxima, current speed peaked in the region south of the Southern ACC front, suggesting that the Polar Front shifted ~5° southward. We propose that the low-frequency ACC frontal migration is primarily controlled by eccentricity-driven shifts in the Southern Hemisphere Westerlies, while precession-driven shifts contribute to high-frequency migration. Our findings imply under future orbital-scale scenarios, the ACC position is likely to shift north.

The Antarctic Circumpolar Current (ACC), the largest current system on Earth[1], flows eastward between ~45°S and ~70°S, encircling the Antarctic continent. Its isopycnal surfaces tilt meridionally from the upper ocean to deeper waters, establishing strong linkages between the surface ocean and nutrient- and CO_2-enriched deep water. This dynamic enhances the nutrient supply for biological productivity and facilitates the exchange of CO_2 between ocean and atmosphere[2]. There are five major oceanographic fronts for the ACC[3-5], with subsidiary fronts related to the northern/southern extents of mean frontal positions (Fig. 1). Each of these fronts, extending from the sea surface to the seafloor[5], with the latitudinal positions changing

seasonally, interannually, and orbitally[6-8], is uniquely important in shaping the behavior and dynamics of the ACC[5].

Significant concern has been raised for the future ocean and climate regarding the possibility of changes in ACC's position. This concern remains, as models and observations present different results, including a poleward shift[9-11] and no change[12]. To quantitatively separate the relative contribution of anthropogenic forcing from natural climate variability, the duration of instrumental observations is obviously too short. Improved prediction of future ACC behavior would rely on long-term records that can provide insights into the strength and position of the ACC during the pre-Anthropocene era,
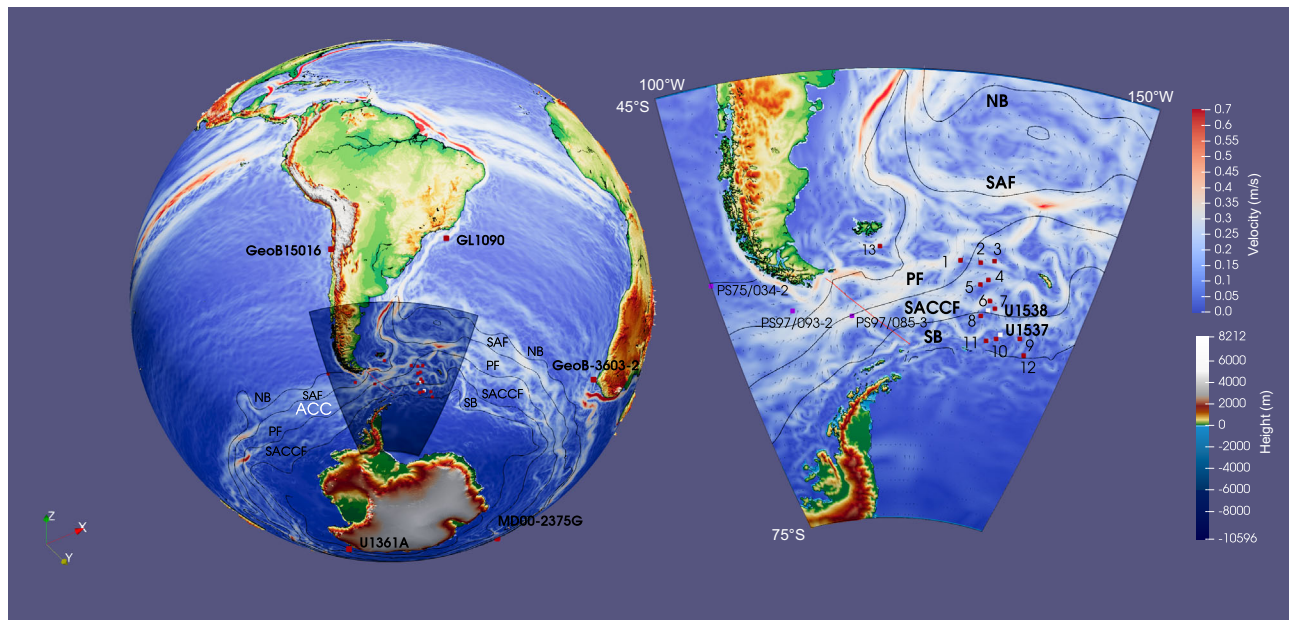
Fig. 1 | Location map. The maps using the MDT_CNES_CLS18_global data set[106] show the global ocean surface current, with warmer red colors representing higher current speeds. Sites U1537 and U1538 are located in the southern Scotia Sea[20,21] (white rectangle). Other red and purple rectangles are sediment sites discussed in this study. The sites, numbered 1 to 13, are as follows: (1) TPC063, 3956 m, (2) TPC077, 3774 m, (3) PS2514-1, 2537 m, (4) PS67/197-1, 3837 m, (5) TPC290, 3826 m, (6) PS67/205-2, 3790 m, (7) PS67/219-1, 3619 m, (8) PS67/224-1, 2868 m, (9) TPC288, 2864 m, (10) PS67/186-1, 3671 m, (11) PS2319-1, 4323 m, (12) TPC287, 1998 m, and (13) GC528, 598 m. The black lines indicate the five main Antarctic Circumpolar Current (ACC) fronts, which from North to South comprise: the North Boundary (NB), the Subantarctic Front (SAF), the Polar Front (PF), the Southern ACC Front (SACCF), and the southern boundary (SB) of ACC, respectively[3,5]. The red line marks the Jason Track 104 near the Drake Passage (DP)[45]. The shaded area in the left map shows the study area (right figure).

particularly during previous warm interglacial periods such as the Last Interglacial (LIG, 128–113 ka)[13,14], when global mean annual temperatures were estimated to be 1.0–1.5 °C higher than preindustrial level[15,16], while global mean sea levels were 6–9 m higher than present[17] (i.e., indicating greater melt contributions from the Antarctic Ice Sheets compared to today). Here, we aim to elucidate the natural forcing for the configuration and reorganization of the ACC frontal systems at orbital timescales, which has profound implications for ACC variability and its interactions with the ocean-atmosphere-cryosphere systems.

The Drake Passage is a crucial bottleneck for the eastward flow of the ACC, connecting the Pacific and Atlantic Oceans[18]. Due to the narrow width and topographic constraint of the Drake Passage, the migration of the ACC is significantly restricted and mesoscale eddies are quite active[19]. In contrast, the Scotia Sea, located downstream of the Drake Passage, is an open basin characterized by a broader and more dispersed frontal system, making the Scotia Sea an ideal location for tracking the ACC intensity changes associated with front migration and its potential impact on the climate system.

Here, we present two reconstructed bottom current speed records extending over ~160 ka from International Ocean Discovery Program (IODP) Sites U1537 (59°6.65′S, 40°54.37′W, 3713 m water depth) and U1538 (57°26.52′S, 43°21.47′W, 3131 m water depth) within the Scotia Sea sector of the Southern Ocean[20,21] (see Fig. 1, core material, and grain-size measurements in Materials). These sites are located within and south of the Southern ACC Front (SACCF), respectively, and are more sensitive to frontal migration than the ACC mainstream. In addition, the interaction between ACC frontal migration and the Antarctic ice sheet is more direct and intense in this region. Age models for Sites U1537 and U1538 are well-constrained through the correlation of high-resolution magnetic susceptibility or Ca counts with the Antarctic European Project for Ice Coring in Antarctica (EPICA) Dome C (EDC) dust or non-sea-salt (nss) Ca^{2+} flux records[21–24] (Supplementary Figs. 1 and 2,

Supplementary Table 1, and age model in Materials). The average temporal resolutions of Sites U1537 and U1538 are 0.8 kyr/sample and 1.8 kyr/sample, respectively, which enables the reconstruction of ACC changes on orbital timescales, rather than focusing on millennial-scale changes that predominantly occurred during the last glacial period. By comparing our reconstructed bottom current records with previously reported data from other locations in the Scotia Sea and Drake Passage, as well as synthesizing atmospheric and oceanic archives from other regions of the Southern Ocean, we elucidate the temporal pattern of ACC migration and provide possible mechanisms, to gain a deeper understanding of its interaction with the dynamic ice-ocean-climate system. Our results reveal that the ACC migration is driven synergistically by eccentricity and precession cycles, with natural forcing likely prompting a northward shift in the ACC position on forthcoming orbital time scales.

Results and discussion
ACC-dominated changes in grain size proxies
The near-bottom current intensity at Sites U1537 and U1538 was reconstructed by using the sortable silt mean grain size ($\overline{SS}$, 10–63 μm) of the terrigenous sediment fraction (Supplementary Figs. 3 and 4). $\overline{SS}$ and mean grain size of sortable silt plus fine sand fractions ($\overline{SSFS}$, 10-125 μm) have been successfully utilized as proxies of variations in near-bottom flow speeds in deep-sea sediments[25–28]. Strong correlation between $\overline{SS}$ and SS% (percentage of sortable silt), as well as between $\overline{SSFS}$ and SSFS% (percentage of sortable silt plus fine sand) indicate that the sediments have undergone current-sorting[26,28]. In high-flow environments like the Drake Passage, ACC can achieve velocities of 40–60 cm/s at depths of ~3000 m, as revealed by mooring observations[29]. These elevated flow velocities are capable of transporting both silt and fine sand fractions, thereby enhancing the sorting process and extending it beyond the conventional sand-silt boundary. Consequently, the $\overline{SSFS}$ serves as a proxy for ocean current strength[28]. However, the

Scotia Sea exhibits moderate bottom water flow velocities, leading to a less pronounced sorting effect. This contrast between the Drake Passage and the Scotia Sea is corroborated by sedimentary analysis, indicating that terrestrial particle sizes are relatively smaller in the Scotia Sea compared to those in the Drake Passage[28,30]. Therefore, for Sites U1537 and U1538, where bottom current velocities are relatively low, $\overline{SS}$ proxy is more suitable for reconstructing bottom current strength.

Icebergs calved from the Antarctic Ice Shelf are thought to have the potential to transport and release terrigenous sand fractions into the Scotia Sea during their drift and melting processes. These unsorted ice-rafted debrises (IRD, >150 μm) may be reworked by bottom currents[31], which could potentially influence the $\overline{SS}$-based flow speed proxy. However, the volume percentage of grains larger than 125 μm is negligible (approaching zero) and the percentage of grain size larger than 63 μm is less than 5% (Fig. 2e and Supplementary Fig. 3e). This suggests that $\overline{SS}$ changes are largely independent of fluctuations in IRD. Meanwhile, the strong positive correlation between $\overline{SS}$ and SS% ($R^2_{U1537} = 0.93$; $R^2_{U1538} = 0.82$) indicates that the sortable silt fraction in all analyzed sediments is effectively sorted by current processes[25] (Supplementary Figs. 5 and 6).

Antarctic Bottom Water (AABW) sourced from the Weddell Sea can be transported to the Scotia Sea through the Orkney Passage via the northern limb of the Weddell Gyre[32] (see oceanographic setting of the Scotia Sea in Materials), potentially influencing the sortable silt fraction. However, dissolved oxygen concentration data, overlain with neutral density contours (γ^n), from the 2013 Annual World Ocean Atlas by Ocean Data View, indicates that Sites U1538 and U1537 are primarily bathed by the Lower Circumpolar Deep Water (LCDW)[33,34] (Supplementary Fig. 7). Furthermore, the temporal changes in $\overline{SS}$ at Site U1538, located at a relatively shallow depth (3131 m) within the SACCF, exhibited a similar pattern to previously published ACC records for the past 30 ka by using $\overline{SS}$ at nearby Site PS67/219-1[30] (Fig. 2b), and for the past 140 ka by using $\overline{SSFS}$ at Site PS97/085-3 (3090 m) around the PF[28] (Supplementary Fig. 8). Such a concordant pattern suggests that $\overline{SS}_{U1538}$ is well representative of the ACC signal. Similarly, $\overline{SS}$ at Site U1537, located further south in the Scotia Sea at a water depth of 3713 m, shows a consistent temporal pattern with $\overline{SS}_{U1538}$ and other ACC records inferred by $\overline{SS}_{PS67/186-1}$[30], $\overline{SS}_{PS97/093-2}$[35] and $\overline{SSFS}_{PS97/085-3}$[28] (Fig. 2c; Supplementary Figs. 8 and 9), but it deviates from the AABW signature[36–40] (see Supplementary Fig. 10). Previous studies proposed that Weddell Sea-derived AABW export was strong during the Holocene but weak during the LIG[36]. However, $\overline{SS}$ values at Sites U1537 and U1538 peaked during the LIG but were low in the Holocene (Supplementary Fig. 10). This discrepancy argues against AABW being the primary control on $\overline{SS}$ variability. Even if AABW influenced Sites U1537 and U1538 during the Holocene, its effects on $\overline{SS}$ values would likely be small given the low flow velocities recorded at both sites during this interval. In addition, AABW transport is suggested to be enhanced during Heinrich Stadials (HS)[37–43], especially during glacial-interglacial transitions (HS 1 and HS 11)[36]. Although the limited sampling resolution at Sites U1537 and U1538 may not fully resolve millennial-scale variability, neither site shows clear evidence of enhanced Heinrich Stadials in $\overline{SS}$ variations on millennial timescales (Supplementary Fig. 10). This further indicates that AABW is not the dominant driver of dynamic changes at these two sites. Taken together, these lines of evidence collectively suggest a predominant influence of ACC on $\overline{SS}$ at these sites. Although the temporal pattern of ACC is consistent across different locations, such as U1537, U1538, and PS97/085-3, the intensity of ACC was likely distinct at different sites, for example, $\overline{SS}_{U1537}$ (14.1–23.6 μm), $\overline{SS}_{U1538}$ (14.9–25.7 μm) and other stations shown in Fig. 3, according to the range of mean value of grain size.

ACC accelerated and poleward shifted during the Last Interglacial

The $\overline{SS}$ record at Site U1537 located south of SACCF is relatively low during the Penultimate Glacial Maximum (PGM, 158–135 ka), with an average $\overline{SS}$ of 16.3 ± 1.2 μm (Fig. 2c and Supplementary Table 2). In comparison, the $\overline{SS}$ record at Site U1538 located within the SACCF is slightly higher, with an average $\overline{SS}$ of 17.8 ± 1.2 μm during the PGM (Fig. 2b). Both $\overline{SS}$ at Sites U1537 and U1538 converged, displaying identical peak values over the full LIG interval (average $\overline{SS}_{U1537} = 21.5 \pm 1.8$ μm; average $\overline{SS}_{U1538} = 21.5 \pm 1.6$ μm), with peak values occurring around 120–113 ka (Fig. 2b, c). The $\overline{SS}$ record at Site U1538 gradually decreased throughout the subsequent glacial period, reaching a minimum at ~15 ka before increasing to a higher value during the Holocene (average $\overline{SS}_{U1538-Holoecne} = 19.0$ μm ± 0.8 μm; Fig. 2b). Conversely, the $\overline{SS}$ record in Site U1537 exhibited a steady decline until ~70 ka, after which it stabilized with minor fluctuations (Fig. 2c). It is worth noting that the Holocene $\overline{SS}$ values at Site U1538 only show a slight increase relative to the Last Glacial Maximum (LGM, 26–19 ka; average $\overline{SS}_{U1538-LGM} = 16.6 \pm 0.3$ μm) and the $\overline{SS}$ at Site U1537 for the Holocene and LGM are relatively low and nearly identical (average $\overline{SS}_{U1537-LGM} = 16.20.3$ μm; average $\overline{SS}_{U1537-Holoecne} = 16.1 \pm 0.5$ μm) regardless of the 11 °C Antarctic air temperature contrast between the Holocene and the LGM and 12 °C difference between the LIG and PGM[44] (Fig. 2a–c; Supplementary Fig. 11). According to the flow-speed calibration of sortable silt for the Scotia-Weddell Sea region[26,27], bottom flow speeds at Site U1538 (14.7 cm/s) and U1537 (14.7 cm/s) were highest during the LIG. These speeds are nearly three times higher than those observed at Site U1537 during the Holocene, LGM, and PGM, which were 5.0 cm/s, 5.3 cm/s, and 5.5 cm/s, respectively (Fig. 2d). Notably, the exceptionally high flow velocities during the LIG contrast sharply with the subdued values recorded during the Holocene. Although both the Southern Ocean sea surface temperatures and Antarctic air temperatures exhibit typical interglacial climatic features, i.e., similar temperature conditions during the LIG and the Holocene, our records reveal a significant contrast in the hydrological behavior of the ACC between these two periods.

To elucidate the reasons behind the low flow velocity observed at Sites U1537 and U1538 during the Holocene, particularly at the southern Site U1537, we integrated our results with other published sortable silt data from Scotia Sea cores and calculated flow speeds[26,27,30]. These reconstructions reveal an overall north-to-south declining trend across the Scotia Sea, with a high velocity of up to 12 cm/s at the northern front, gradually decreasing to ~5 cm/s towards the south (Fig. 3h). In order to further establish linkages between Holocene flow structures and modern frontal configurations, we compared our records with contemporary velocity transects (Fig. 3h). The Jason Track 104 transect in the Drake Passage exhibits a constricted ACC structure with enhanced mesoscale eddy activity due to topographic constraints[45]. In contrast, ACC fronts near Sites U1537 and U1538 within the Scotia Sea display greater zonal dispersal and reduced eddy activity. To minimize regional biases in modern observational data and ensure spatial consistency with sediment core locations, we utilized satellite altimetry-derived flow velocity data for the Scotia Sea region. The observational data in the Scotia Sea shows greater volume transport and higher current velocities associated with the ACC around the southern subsidiary of the Subantarctic Front (SAF), the Polar Front (PF), and SACCF[18,46]. In contrast, the flow velocity significantly weakens in the region south of the SACCF (Fig. 3h)[18,46]. Considering that the reconstruction results of this study reflect a long-term mean state, while modern observational data encompass high-frequency variability from interannual to subannual scales, we calculated the trend of modern flow velocity data to facilitate comparison with Holocene reconstructions. Overall, the Holocene reconstructed flow velocities in the Scotia Sea exhibit a spatial pattern that is highly consistent with modern
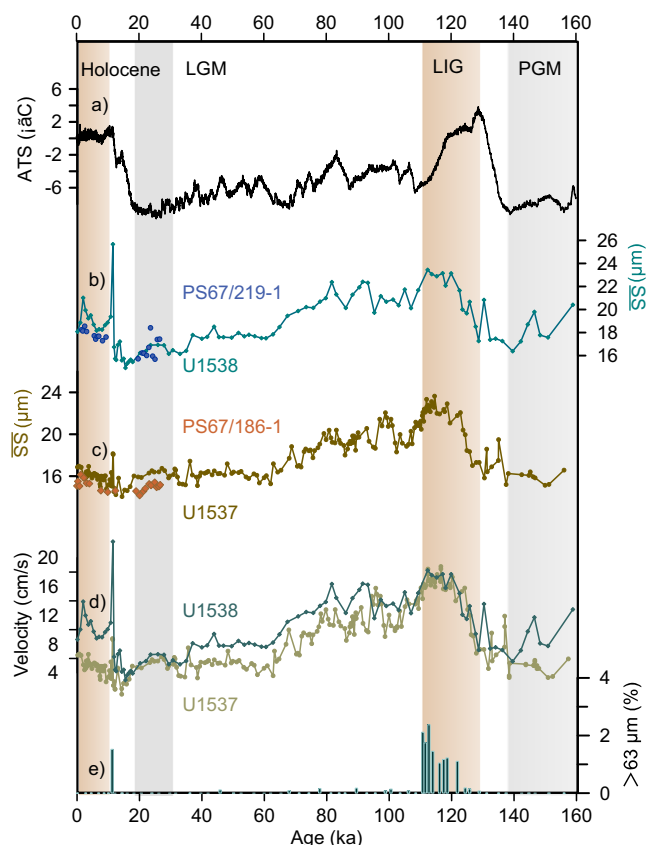
Fig. 2 | **Reconstructed changes in current strength and the associated paleo-climate for the past 160 ka. a** Antarctic Temperature Stack (ATS)[44]. **b** Sortable silt mean grain size ($\overline{SS}$) at Sites U1538 (this study) and PS67/219-1 (Core 7 in Fig. 1)[30] in the Scotia Sea. **c** $\overline{SS}$ at Site U1537 (this study) and PS67/186-1[30] (Core 10 in Fig. 1) in the Scotia Sea. **d** Bottom flow speeds calculated by $\overline{SS}$ from Sites U1537 and U1538 (this study)[26,27]. **e** The percent of grain size larger than 63 μm at Site U1537. LGM: Last Glacial Maximum, LIG: Last Interglacial, PGM: Penultimate Glacial Maximum.

observations ($r = 0.72$, $p = 0.01$; Fig. 3h). This result not only confirms the reliability of the reconstruction data in capturing key spatial features of the Holocene ACC but also explains the sustained low flow velocities at the southernmost Site U1537 during the Holocene.

Relative to Holocene, ACC speeds during the LGM were lower at multiple locations in the main fronts of the Drake Passage and the Scotia Sea, for example, decreased by 4.0 cm/s at Site PS97/093-2 (~40 km NW of the SAF; 3781 m)[35], 5.1 cm/s at Site PS97/085-3 (~40 km north of the PF; 3090 m)[28], 4.4 cm/s at Site U1538 (SACCF) (Fig. 3b, d and e; Supplementary Fig. 12). This LGM decrease in ACC can be observed even at the central South Pacific (Fig. 3d)[47]. However, the ACC velocities at Site U1537, located south of the SACCF in the Scotia Sea, were found to be low both in the LGM and the Holocene (Fig. 3f and Supplementary Fig. 12), and this relatively stable and low current velocities phenomenon had been reported previously in the Scotia Sea[30]. The above compilation suggests that the ACC intensity reduced considerably during the LGM, while the general configuration of the ACC front in the Scotia Sea and the Drake Passage remained relatively stable. This inference is further supported by similar flow speed patterns observed across the Scotia Sea transect[30] (Supplementary Fig. 11).

During the stabilized interval of the LIG (123–118 ka), there was a widespread increase in current speed encompassing the fronts within the Drake Passage and Scotia Sea compared to the Holocene. For locations in the Pacific entrance to the Drake Passage ~40 km NW of the SAF (PS97/093-2, 3781 m)[35] and in the central Drake Passage ~40 km north of the PF (PS97/085-3, 3090 m)[28], the current speed increased by

1.2 cm/s (5.5%) and 2.9 cm/s (8.4%), respectively (Fig. 3i and Supplementary Fig. 12). Interestingly, these increments are relatively small compared to the ones at Site U1538 (increased by 6.0 cm/s or 58.3%) near the SACCF and U1537 (increased by 10.6 cm/s or 211.0%) south of the SACCF in the Scotia Sea (Fig. 3i and Supplementary Fig. 12). Notably, an increase in current speed was also recorded in the pelagic central South Pacific[47] (Fig. 3c), suggesting that the basin-wide acceleration of currents during LIG extended beyond the Drake Passage and the Scotia Sea. The increasing ACC velocity with latitudes, particularly pronounced at the southernmost stations (Fig. 3i), indicates that ACC acceleration (ACC volume transport increase) alone cannot fully explain the spatial pattern. If only ACC volume transport increase had occurred, as observed during the Holocene relative to the LGM, significant velocity changes would be expected across the main fronts, with only minor changes near the southern boundary of the ACC in the Drake Passage and the Scotia Sea. Instead, the stronger ACC increases observed toward the south point to a poleward shift of the ACC fronts during the LIG. The relatively modest increases in current speed observed at Drake Passage (e.g., Sites PS97/093-2[35] and PS97/085-3[28]; see Fig. 3i) may be attributed to a reduced influence of frontal shifts, which are constrained by topographic features.

The poleward migration of the ACC fronts is supported by several lines of evidence. For example, the synchronous warming in sea surface temperature (SST) records at both the southeast Pacific (Site PS75/034-2) and the southwest Atlantic (Site GL1090) during the LIG relative to the Holocene[48,49] is supportive (Fig. 3i and Supplementary Fig. 13). As the poleward movement of the ACC fronts would enhance the exchange of water masses between the Pacific and Atlantic, the temperature disturbance upstream of the Drake Passage and the Scotia Sea would be propagated promptly to areas downstream of the Drake Passage[45,50]. Meanwhile, synchronous slowdowns of ACC flow speed further north of SAF in the Indian open ocean zone of the Southern Ocean (Site MD00-2375G; Fig. 3a and i)[51] and at the Agulhas Plateau Composite near ACC northern boundary[52], is also supportive of ACC poleward migration, as a pronounced southward shift of the ACC fronts would reduce northern ACC volume transport[35]. Independent evidence from the Cape Basin, where planktonic foraminifera records reveal a southward shift of the Subtropical Convergence[53] (Site GeoB3603-2; Fig. 3i and Supplementary Fig. 13), further corroborates the large-scale ACC poleward migration during the LIG.

Interestingly, the current velocity at Site U1537 and Site U1538 during the stabilized interval of the LIG is identical to the current speed at Site BAS TPC06, located south of SAF. If we assume that the distribution pattern of the bottom flow speeds across the fronts remained consistent over time, it is plausible that the position of the Holocene PF at Site BAS TPC063 may have shifted southward to Site U1537 during the LIG. Given the latitudinal difference between Site U1537 and Site BAS TPC063, it can be inferred that the PF in the Scotia Sea may have shifted poleward by ~5°. Although this approach may simplify the potential variability in ocean circulation over time, including the effects of varying climatic conditions on circulation it is corroborated by other reconstructions derived from SST records from the Atlantic and Indian Ocean sectors of the Southern Ocean[54–58] (Supplementary Fig. 14). The 5° poleward movement of the PF would likely enhance the intrusion of Circumpolar Deep Water onto the Antarctic shelves, leading to de-stabilization and mass loss of the Antarctic Ice Sheets from underneath by ocean thermal forcing[31], influencing global-mean sea level, ocean circulation, and global climate[59–61].

Eccentricity and precession modulate ACC fronts migration

Changes in the Earth's orbital parameters exert a significant influence on the seasonal and spatial distribution of solar insolation[62], potentially affecting the position of ACC fronts[47,63]. Low-frequency variability of $\overline{SS}$ at Site U1537 is synchronous with orbital eccentricity[64], with the highest $\overline{SS}$ observed during periods of maximum eccentricity in the
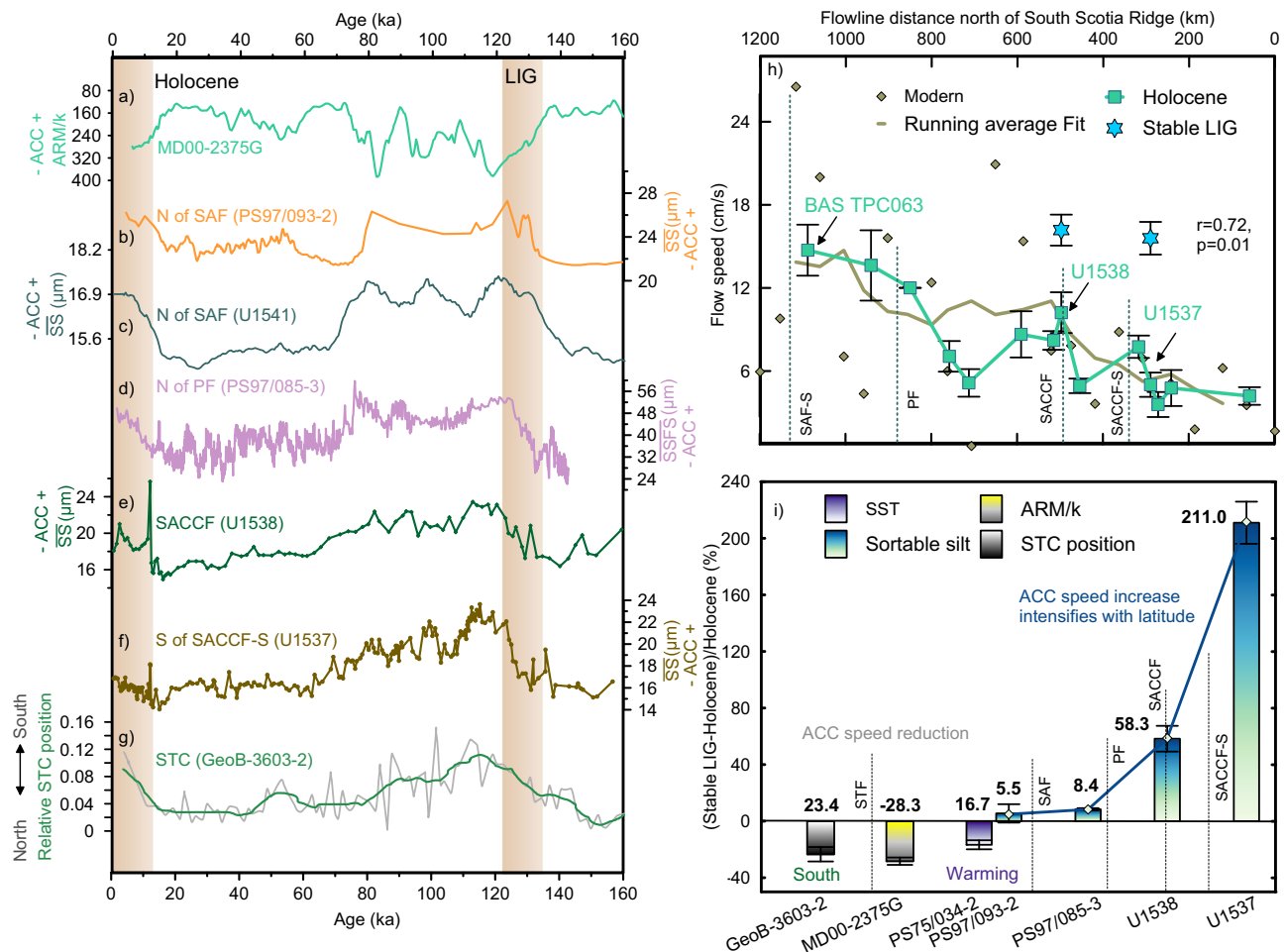
Fig. 3 | Comparison of ACC flow speed in different regions and related paleoclimate records. a Antarctic Circumpolar Current (ACC) flow speed inferred by the ARM/*k* at Site MD00-2375G[51]. **b** $\overline{SS}$ from PS97/093-2[35]. **c** $\overline{SS}$ from U1541[47]. **d** Mean grain size of the sortable silt plus the fine sand fractions ($\overline{SSFS}$, 10–125 μm) from PS97/085-3[28]. **e**, **f** $\overline{SS}$ at Sites U1538 and U1537, respectively (this study). **g** Relative Subtropical Convergence (STC) position in the Cape basin based on planktonic foraminifer data[53]. **h** Modern mean surface velocities from satellite data (light grey diamonds) and their 5-point running mean (light grey line)[46] and the bottom flow speeds calculated by $\overline{SS}$ at the transect across the Scotia Sea[30] during the Holocene (sea green line). Holocene average values are shown as sea green boxes, and Stable Last Interglacial (LIG) average values are shown as blue stars, with error bars indicating one standard deviation. **i)** Bar chart comparing sea surface temperature (SST[48], current speed[28,35,51], and STC position proxies[53] across the front during the stable LIG. Each bar represents the absolute value of the relative percent change between the Stable LIG and the Holocene (shown in bold), with error bars indicating the estimated uncertainty of the relative difference.

LIG, and the lowest $\overline{SS}$ recorded during periods of minimum eccentricity in the Holocene and LGM (Fig. 4a, b). After removing the long-term $\overline{SS}$ trend of U1537 associated with eccentricity, the detrended $\overline{SS}$ exhibits a distinct precessional signal with larger $\overline{SS}$ occurring for precession maxima when the orbital precession amplitude reaches its highest value[65,66], and vice versa for precession minima (Fig. 4c). Furthermore, wavelet analysis[67] and the cross-wavelet transform (XWT) spectrum[68] also reveal a marked precessional variability with a period of 22 kyr (Supplementary Figs. 15 and 16). A similar precession cycle is also observed at Site U1538, as shown in the detrended $\overline{SS}$ record and corroborated by the XWT analyses (Supplementary Figs. 16 and 17). This precession signature aligns with the variability observed in the ACC record from Site MD00-2375G[51], situated near the northern boundary of the ACC (Fig. 4f). Collectively, these findings suggest that ACC front migration is closely associated with orbital precession and eccentricity variation.

Moreover, we observed that the inferred ACC shifts do not fully align in time with the LIG as revealed in temperature proxies[44]. Specifically, while peak interglacial temperatures generally occurred at ~128–118 ka, the largest ACC shifts are observed later at ~120–113 ka (Fig. 2). This difference underscores the distinct hydrological behavior

of the ACC, and thus further indicates that a dominant orbital forcing over the imprint of the glacial-interglacial cycle.

A plausible mechanism for the ACC front migration may involve the modulation of Southern Hemisphere Westerlies (SHW) by orbital precession[69,70], which is further amplified by variations in eccentricity. As orbital eccentricity influences the overall intensity of solar insolation by altering the Earth's distance from the Sun and modulating seasonal contrasts, superimposed orbital precession further amplifies these effects by changing the distribution and intensity of insolation differences between the Southern and Northern Hemispheres. The subsequent changes in the interhemispheric insolation gradient lead to a shift in Intertropical Convergence Zone (ITCZ) movement[71,72], which in turn impacts the strength and position of SHW[73–75], and subsequently ACC frontal movement[9,76]. Notably, during the LIG, when orbital eccentricity and precession reached their maxima, with perihelion occurring during Southern Hemisphere summer, the resulted maximum Southern Hemisphere insolation, coupled with reduced Northern Hemisphere insolation, likely intensified interhemispheric temperature gradients. This enhanced meridional temperature gradient would amplify shifts in the SHW, driving the ACC to its
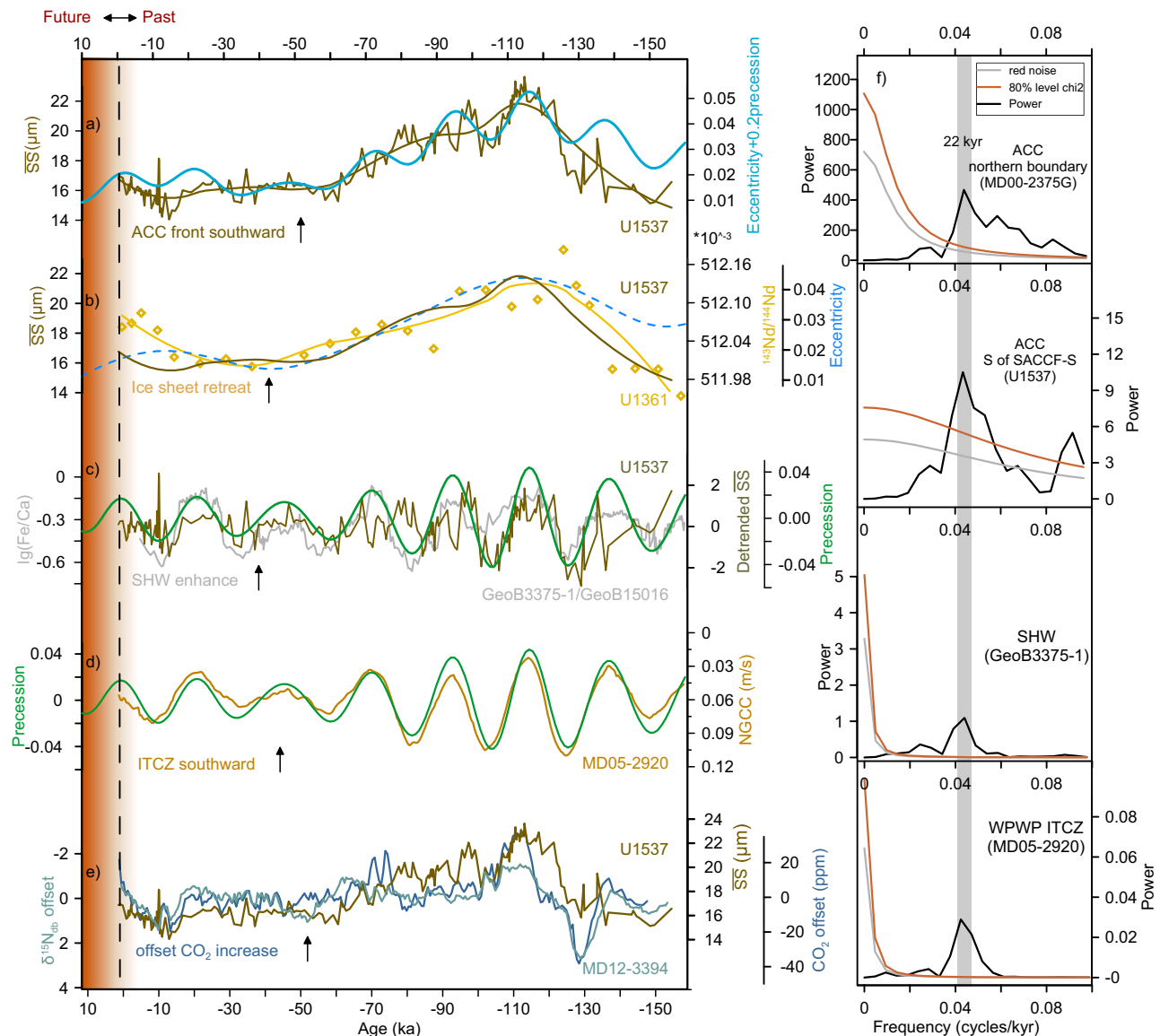
Fig. 4 | Orbital change in ACC fronts and the associated paleoclimate records.
a Sortable silt mean grain size ($\overline{SS}$) and the loess $\overline{SS}$ at Site U1537 (this study), and (eccentricity+0.2precession)[64]. **b** Loess $\overline{SS}$ at Site U1537, eccentricity[64], and Antarctic Ice Sheet change inferred by detrital sediment Nd isotopes records at Site U1361A[87]. **c** Precession[64], detrended $\overline{SS}$ at Sites U1537, and Southern Hemisphere Westerlies (SHW) inferred by log (Fe/Ca) at Site GeoB3375-1/GeoB15016[73]. **d** Precession[64] and the movement of the Western Pacific Intertropical Convergence Zone (ITCZ) inferred by the simulated New Guinea Coastal Current (NGCC) at Site MD05-2920[79]. **e** $\overline{SS}$ at Site U1537, $\delta^{15}N_{db}$ offset record calculated using the $\delta^{15}N_{db}$ at Site MD12-3394[95], and CO_2 offset record[95,96]. **f** Spectral analysis of detrended ARM/k records at Site MD00-2375G[51], detrended $\overline{SS}$ records at Site U1537, SHW inferred by log(Fe/Ca)[73], and the movement of the Western Pacific ITCZ inferred by the simulated NGCC at Site MD05-2920[79].

southernmost position and accelerating flow at both Sites U1537 and U1538, with a more pronounced acceleration observed at U1537 due to its more southerly location. Conversely, during periods of low eccentricity, e.g., the Holocene, the overall weaker insolation contrasts likely decreased the interhemispheric temperature gradients, resulting in a more northerly position of the ACC and slower flow at Sites U1537 and U1538 (with U1538 exhibiting greater flow than U1537), similar to present-day conditions.

This hypothesis is further corroborated by the consistent precessional variability exhibited in the detrended $\overline{SS}$ at Sites U1537 and U1538, the SHW reconstructions[73,77,78], and the ITCZ records in the Western Pacific Warm Pool[79] (Fig. 4c, d, f), pointing to a potential linkage between ACC frontal migration and tropical climate. Furthermore, the reconstructed ACC strength over the past five million years exhibits eccentricity cycles[47], corroborating our findings. The overall

temporal variation pattern of U1537 $\overline{SS}$, most consistent with the combination of eccentricity and a 0.2 times precession, suggest that the low-frequency eccentricity potentially acts as the primary natural forcing and precession as the secondary means (Fig. 4a). It is worthwhile to note that the natural forcing would move ACC northward in the coming era (i.e., during the next 10,000 years) due to orbital change.

In contrast to the overall orbital-scale trend, the $\overline{SS}$ during both the pre--130 ka and 70–80 ka intervals appear to deviate slightly from the orbital forcing. When comparing Antarctic ice core temperature reconstructions, we find consistent co-variation between $\overline{SS}$ and temperature[44] during these two periods (Supplementary Fig. 18). This might reflect a response of ACC to other factors, e.g., temperature, rather than orbital forcing. However, the specific mechanisms require further investigation.

Potential impact of ACC frontal changes on polar upper nutrient supply

Modern observations and paleoclimate records have revealed tropical teleconnections to high latitudes climate on interannual, centennial to millennial timescales[80–82], while some studies propose the opposite scenario[83–85]. Our study suggests the orbital-scale shifts in the ACC front are linked to tropical climate variability, as evidenced by the coherent precessional signals observed in the detrended $\overline{SS}$ records from Sites U1537 and U1538, the SHW reconstructions[73], and the Western Pacific hydroclimate records[71,72] (Fig. 4c, d, f). As global warming intensifies, the ACC's position has gained attention for its role in modulating ice-sheet stability through ocean heat transport and sub-ice shelf melting[86]. Our sites, located around and south of the SACCF, lie within a region where the ACC interacts more directly with the Antarctic Ice Sheet. The variability patterns identified in our records broadly align with changes observed in the East Antarctic Ice sheet[87] (Fig. 4b), indicating a strong coupling between these systems, with orbital-scale shifts in the ACC front possibly playing a crucial role in driving these interactions. However, we also observed a decoupling between U1537 $\overline{SS}$ and Antarctic Ice Sheet variability inferred from Site U1361A (Fig. 4b) during the Holocene. This discrepancy may stem from heterogeneous responses of the Antarctic Ice Sheet to oceanic warming or circulation shifts, e.g., reinvigoration of the Atlantic Meridional Overturning Circulation and the subsequent increase in the intrusion of CDW[88], whose underlying mechanisms remain unclear and merit further investigation.

Given the ACC's role as a crucial component of the Southern Ocean overturning circulation[89], the latitudinal shifts of ACC fronts may affect the upper nutrient supply, productivity, and atmospheric CO_2 concentration for biogeochemical cycles and climate change[55,90,91]. Modeling studies suggest a potential link between SHW changes and atmospheric CO_2 concentrations[92–94], wherein shifts in SHW intensity and position may affect deep-water upwelling, thereby influencing nutrient dynamics and CO_2 release. As orbital eccentricity and precession modulate SHW patterns[69,70], the resulting ACC front shift could play a key role in regulating these processes. The consistency of U1537 $\overline{SS}$ with $\delta^{15}N_{db}$ records in the Antarctic Zone, as well as CO_2 offset records ($r = 0.56$, $n = 149$, $P < 0.01$; $r = -0.47$, $n = 149$, $P < 0.01$, respectively; Fig. 4e and Supplementary Fig. 19), which were derived from subtracting the temperature component after a linear regression between the $\delta^{15}N$/atmospheric CO_2 composite and Antarctic temperature stack[95,96], is particularly evident during the LIG when both eccentricity and precession reached maximum values. Specifically, $\delta^{15}N_{db}$ records show minimum values, while U1537 $\overline{SS}$ and CO_2 offset records reach their maxima (Fig. 4e), supporting the assertion that the migration of ACC fronts is dynamically linked to upper nutrient supply, productivity, and atmospheric CO_2 concentration. During the LIG, peak orbital eccentricity and precession intensified and shifted the SHW southward, likely triggering a southward migration of the ACC, which in turn shifted the upwelling center and induced the upwelling of deep-water mass with higher nutrients and CO_2 to the surface, consequently enhancing nutrient concentration, productivity, and releasing oceanic CO_2 towards the south.

A southward shift and significant intensification of the SHW have been observed over the past decades in response to global warming[11]. It is projected that the ACC position may undergo a substantial southward shift in the future, as the intensified SHW persist[9,10]. Considering the decreasing trend in eccentricity and precession, it is reasonable to infer that the ACC position would gradually shift northward under natural conditions in the future (i.e., during the next 10,000 years) (Fig. 4a). However, the interaction between the insolation and oceanic dynamic over time remains uncertain, and any potential interactions between these processes would depend on their relative magnitudes, which differ significantly, and their temporal overlap. Current Argo float drift observations suggest that, at least in the short term, the ACC position has experienced only minor changes[12]. Given the complexities and uncertainties surrounding the interaction of these processes, to accurately project the ACC's dynamic behavior, including its strength and position, and gain insights into the global climate system in greenhouse scenarios, it is crucial to consider the complex interaction of natural variability and human-induced factors, and thus a combination of paleoceanographic records and models will be essential in the future.

Methods

Core material

In this study, we applied spliced sediment cores from Site U1537 (59°6.65'S, 40°54.37'W, water depth: 3713 m) and U1538 (57°26.52'S, 43°21.47'W, 3131 m water depth) in the Scotia Sea[20,21] to reconstruct ACC strength over the past 160 ka. The spliced sediment cores were collected from the IODP Expedition 382 "Iceberg Alley" during 2019[20,21]. Site U1537 is located in the Dove Basin, southern Scotia Sea, and Site U1538 is located in the Pirie Basin, northern Scotia Sea. For this study, we focus on three long holes drilled at Site U1537. Hole U1537A was drilled to a depth of 264.0 m CSF-A, with a total core recovery of 268.9 m (102%), and we used the depth interval 5.59–31.467 m CCSF, corresponding to an age range of 11.13–133.0 kyr on the AICC2012 chronology. Hole U1537B was drilled to 7.4 m CSF-A with a 100% recovery, and we used the interval 0.05–5.95 m CCSF, corresponding to 0.29–11.76 kyr. Hole U1537D was drilled to 354.3 m CSF-A, with a total recovery of 349.0 m (99%), and we used the interval 10.98–34.538 m CCSF, corresponding to 31.08–156.16 kyr. For Site U1538, we focus on three long holes as well. U1538A was drilled to a depth of 676.0 m CSF-A, with a total core recovery of 476.43 m (70.48%), and we used the depth interval 0.21–45.59 m CCSF, corresponding to an age range of 0.30–128.83 kyr on the AICC2012 chronology. Hole U1538C was drilled to 105.9 m CSF-A with a 93.41% recovery, and we used the interval 7.86–32.26 m CCSF, corresponding to 12.04–83.22 kyr. Hole U1538D was drilled to 126.4 m CSF-A, with a total recovery of 114.6 m (90.66%), and we used the interval 15.14–53.97 m CCSF, corresponding to 20.38–167.90 kyr.

There are five major oceanographic density gradients, or fronts[3–5], for the ACC from north to south, including the Subtropical Front (STF), the SAF, the PF, the Southern ACC Front (SACCF), and the southern boundary of the ACC (SB), respectively[3–5]. STF and SB mark the northern and southern boundaries of the ACC, respectively[5]. According to the annual mean position of the circumpolar fronts[5], Site U1538 is located around the SACCF (Fig. 1). Site U1537 is located to the south of the SACCF-S and to the north of SB[3,5]. Therefore, these two cores are situated to the South of PF, a location characterized by vigorous upwelling of nutrient- and CO_2-rich LCDW[22,23].

Age model

As the magnetic susceptibility (MS) and Ca records of Site U1537 are the reliable tracers of atmospheric circulation[21–23], the U1537 age pattern relies on a previously published age model[23] that was based on the correlation of Site U1537 MS and Ca^{2+} records to EPICA Dome C (EDC) dust flux records, as well as EDC or East Antarctic Dronning Maud Land (EDML) $nssCa^{2+}$ flux records[21–24]. We constructed the age model of Site U1538 based on the correlation of Site U1538 MS to EDC dust flux records[97] following the methods of Weber et al.[22,97] and Lu et al. (2022)[23]. A total of 35 tuning points were utilized in the final age model (Supplementary Fig. 1 and Table 1[98]). Age-depth modeling with age uncertainty was performed with the same setting parameters of U1537 using the Undatable MATLAB tool[23,99] (Supplementary Fig. 2). The age control points between the U1538 MS record and the EDC dust flux were based on the AICC 2012 age scale[24,100]. The good agreement between U1538 MS and EDC dust confirms that U1538 MS is qualified to record the Antarctic dust variations similarly to Site U1537, supporting the robustness of our chronology.

Grain-size measurements

Two groups of grain-size measurements for Site U1537 were conducted in our study. Group One measurements included 224 freeze-dried samples with 0.1–0.2 m sampling increments from 0.05 to 34.538 m. These samples were pretreated according to McCave et al.[25] by freeze-drying and adding 30 ml hydrogen peroxide (10%) to remove organic matter[25]. Afterward, the residue was sieved through a 63 μm sieve. Because Site U1537 is located below the carbonate compensation depth, and thus contains little carbonate (calcium carbonate <1 wt%), we did not remove carbonate. Additionally, abundant diatoms and sponge spicules can be seen under the microscope. Because diatoms and sponge spicules could affect the terrigenous particle size spectra, 30 ml (2 mol/l) sodium carbonate solution was used to remove diatoms and sponge spicules in a thermostat water bath at 85 °C for 5 h. We also added 20 ml (0.1 mol/l) sodium hexametaphosphate to avoid grain aggregation. 94 freeze-dried U1538 samples were conducted with 0.3–1.154 m sampling increments from 0.21 to 52.872 m with the same pretreatment.

For better comparison, 70 freeze-dried U1537 samples at 0.1–1.3 m sampling increment from the same interval were pretreated without sieving. All other procedures followed the same protocol as Group one, as described above. Both groups of all of the samples were analyzed for particle grain size using a CILAS 1190L laser diffraction particle-size analyzer in the Key Laboratory of Ocean and Marginal Sea Geology, South China Sea Institute of Oceanology, Chinese Academy of Sciences in Guangzhou, China. The instrument can detect grain sizes ranging from 0.04 to 2500 μm, with an accuracy error of less than 3% and a repeatability error of no more than 1%. Our repeated results showed a high correlation of $\overline{SS}$ in both groups of measurements at Site U1537 ($R_1^2 = 0.99$; $R_2^2 = 1$). Based on the replicated results from 22 samples, the analytical precision was ±0.08 μm in our measurements. For additional details of the results, see the results of grain-size measurements in Materials.

Time-series analysis

Wavelet analysis was performed on the sortable silt mean grain size time series from Site U1537 using a Morlet continuous wavelet transform (CWT)[67]. Cross-wavelet transform (XWT) spectrum analysis was carried out in MATLAB using MATLAB function XWT[68]. Prior to analysis, $\overline{SS}$ at Site U1537 and U1538 were interpolated in the sample rate of 0.5962 kyr and 1.7982 kyr, respectively. Spectral analysis was performed based on the REDFIT method implemented in PAST version 4.07b with the following settings for the analyses: Window = Rectangle; Oversample = 2; Segments = 2[65,101].

The results of grain-size measurements

Group One of Site U1537. Generally, $\overline{SS}$ changed markedly spanning the past 160 ka (Supplementary Figs. 3a and 4a). Specifically, $\overline{SS}$ was stable generally during the Penultimate Glacial Maximum (PGM, 158–135 ka; average $\overline{SS} = 16.3$ μm), while it significantly increased during the LIG (average $\overline{SS} = 21.5$ μm) with the highest peak at 114.7 kyr (23.6 μm). After 114 ka, $\overline{SS}$ decreased gradually, with distinct high peaks during 101.18–97.14 ka, 92.98–90.21 ka, and 83.25–80.93 ka. After 70 ka, $\overline{SS}$ was relatively stable and low until the Last Glacial Maximum (LGM, 26–19 ka; average $\overline{SS} = 16.2$ μm). Interestingly, the average Holocene values are similar to those during the LGM (average $\overline{SS} = 16.1$ μm; Supplementary Table 2). This little change of $\overline{SS}$ between the LGM and the Holocene (average $\overline{SS}_{LGM-Holocene} = 0.1$ μm) is consistent with the nearby Site PS67/186-1 (core 10 in Fig. 1) in the southern Scotia Sea (Fig. 2c)[30]. The comparisons show little change in the average $\overline{SS}$ between the cold PGM and LGM, but the average $\overline{SS}$ during the LIG is distinctly higher than that during the Holocene with a difference of 5.38 μm. There is a highly positive correlation between $\overline{SS}$ and SS% in Group One ($R^2 = 0.93$; Supplementary Figs. 5a and 6a). The

linear correlation coefficient of $\overline{SS}$ in the repeated measurement is 0.99 (Supplementary Fig. 5c).

Group two of site U1537. $\overline{SS}$ and SS% are highly correlated ($R^2 = 0.92$; Supplementary Fig. 5b). A strong correlation of $\overline{SS}$ also occurred in the repeated measurement ($R^2 = 1$; Supplementary Fig. 5d). Change in $\overline{SS}$ over the past 160 ka is similar to the one in Group One (Supplementary Figs. 3a and 3c). Specifically, $\overline{SS}$ during the LIG, PGM, and LGM are approximately equivalent to those in Group One with average values of 21.7 μm, 16.0 μm, and 16.3 μm, respectively (Supplementary Table 2). However, the average of $\overline{SS}$ during the Holocene (average $\overline{SS} = 17.6$ μm) is slightly higher than that in Group One (Supplementary Table 2). In addition, we found that the volume percent of the grains greater than 125 μm is close to 0. The volume percent of the grains greater than 63 μm is low (less than 3%) over the past 160 ka, with two higher peaks during the LIG and 12–11 ka (Supplementary Fig. 3e).

Site U1538. Variation in U1538 $\overline{SS}$ is similar to that of U1537, and the value of U1538 $\overline{SS}$ during the LIG and LGM is nearly identical to U1537 $\overline{SS}$ (Supplementary Fig. 4). Specifically, sortable silt mean grain size increased significantly from PGM (average $\overline{SS} = 17.8$ μm) to LIG (average $\overline{SS} = 21.5$). The Holocene average $\overline{SS}$ (19.0 μm) was also slightly higher than the LGM average $\overline{SS}$ (16.6 μm). There is also a highly positive correlation between $\overline{SS}$ and SS% at Site U1538 ($R^2 = 0.82$; Supplementary Fig. 6b).

Oceanographic setting of the Scotia Sea

The Scotia Sea can be influenced by the eastward flow of the ACC and the northward flow of Weddell Sea Deep Water (WSDW)[102]. The ACC flowing eastward between ~45 and ~70°S tightly connects the Atlantic, Pacific, and Indian Oceans[97]. Circumpolar Deep Water (CDW), representing the largest water mass of the ACC[103], is a mixture of North Atlantic Deep Water (NADW), Antarctic Bottom Water (AABW), and Antarctic Intermediate Water (AAIW). As the eastward ACC flows into the Southeastern Pacific along the SAF, a major fraction of ACC flows through the Drake Passage and the Scotia Sea prior to entering the southern Atlantic, while a minor part branches off and turns north toward the Chilean coast and the equatorial eastern Pacific[104]. There are three principal fronts from north to south that extend from the sea surface to the seafloor within the ACC across the Scotia Sea: the PF, the SACCF, and the SB, respectively[5]. Subsidiary fronts related to the northern/southern extents of mean frontal positions were further identified by satellite altimetry[5]. Higher ACC velocities prevail in the vicinity of the PF, while ACC slows down towards the southern SACCF[45]. The WSDW is an important subset of AABW[105], which we refer to as Weddell Sea-derived AABW. It can outflow at the northeastern end of the Weddell Gyre and enter the Scotia Sea through the Orkney Passage[32].

Data availability

All original data presented in this article are available at https://doi.org/10.5281/zenodo.14907902. Source data are provided with this paper.

References

1. Marshall, J. & Speer, K. Closure of the meridional overturning circulation through Southern Ocean upwelling. *Nat. Geosci.* **5**, 171–180 (2012).
2. Toggweiler, J. R. & Russell, J. Ocean circulation in a warming climate. *Nature* **451**, 286–288 (2008).
3. Orsi, A. H., Whitworth III, T. & Nowlin, W. D. Jr On the meridional extent and fronts of the Antarctic Circumpolar Current. *Deep Sea Res. Part I Oceanogr. Res. Pap.* **42**, 641–673 (1995).
4. Taylor, J. R. et al. Submesoscale Rossby waves on the Antarctic circumpolar current. *Sci. Adv.* **4**, 2824 (2018).

5. Sokolov, S. & Rintoul, S. R. Circumpolar structure and distribution of the Antarctic Circumpolar Current fronts: 1. Mean circumpolar paths. *J. Geophys. Res. Oceans* **114**, C11018 (2009).

6. Pauthenet, E. et al. Seasonal meandering of the Polar Front upstream of the Kerguelen Plateau. *Geophys. Res. Lett.* **45**, 9774–9781 (2018).

7. Sokolov, S. & Rintoul, S. R. Subsurface structure of interannual temperature anomalies in the Australian sector of the Southern Ocean. *J. Geophys. Res. Oceans* **108**, 3285 (2003).

8. Gersonde, R., Crosta, X., Abelmann, A. & Armand, L. Sea-surface temperature and sea ice distribution of the Southern Ocean at the EPILOG Last Glacial Maximum—a circum-Antarctic view based on siliceous microfossil records. *Quat. Sci. Rev.* **24**, 869–896 (2005).

9. Fyfe, J. C. & Saenko, O. A. Simulated changes in the extratropical Southern Hemisphere winds and currents. *Geophys. Res. Lett.* **33**, L06701 (2006).

10. Downes, S. M., Budnick, A. S., Sarmiento, J. L. & Farneti, R. Impacts of wind stress on the Antarctic Circumpolar Current fronts and associated subduction. *Geophys. Res. Lett.* **38**, L11605 (2011).

11. Yang, H. et al. Poleward shift of the major ocean gyres detected in a warming climate. *Geophys. Res. Lett.* **47**, e2019GL085868 (2020).

12. Böning, C. W., Dispert, A., Visbeck, M., Rintoul, S. R. & Schwarz-kopf, F. U. The response of the Antarctic Circumpolar Current to recent climate change. *Nat. Geosci.* **1**, 864–869 (2008).

13. Menviel, L. et al. The penultimate deglaciation: protocol for Paleoclimate Modelling Intercomparison Project (PMIP) phase 4 transient numerical simulations between 140 and 127 ka, version 1.0. *Geosci. Model Dev.* **12**, 3649–3685 (2019).

14. Wang, M. & Zong, Y. Significant SST differences between peak MIS5 and MIS1 along the low-latitude western North Pacific margin. *Quat. Sci. Rev.* **227**, 106060 (2020).

15. Masson-Delmotte, V. et al. A comparison of the present and last interglacial periods in six Antarctic ice cores. *Climate* **7**, 397–423 (2011).

16. Capron, E. et al. Temporal and spatial structure of multi-millennial temperature changes at high latitudes during the Last Interglacial. *Quat. Sci. Rev.* **103**, 116–133 (2014).

17. Dutton, A. et al. Sea-level rise due to polar ice-sheet mass loss during past warm periods. *Science* **349**, aaa4019 (2015).

18. Lamy, F. et al. Glacial reduction and millennial-scale variations in Drake Passage throughflow. *Proc. Natl Acad. Sci. USA* **112**, 13496–13501 (2015).

19. Farneti, R., Delworth, T. L., Rosati, A. J., Griffies, S. M. & Zeng, F. The role of mesoscale eddies in the rectification of the Southern Ocean response to climate change. *J. Phys. Oceanogr.* **40**, 1539–1557 (2010).

20. Weber, M. E., et al. Site U1537, Iceberg alley and subantarctic ice and ocean dynamics. In *Proc. International Ocean Discovery Program*, 382 (2021).

21. Weber, M. E., Raymo, M. E., Peck, V. L., Williams, T., & IODP Expedition 382 Scientists, E. Iceberg Alley and Subantarctic Ice and Ocean Dynamics. In *Proc. International Ocean Discovery Program*, 1–32 (2021).

22. Weber, M. E. et al. Antiphased dust deposition and productivity in the Antarctic Zone over 1.5 million years. *Nat. Commun.* **13**, 2044 (2022).

23. Lu, L. et al. One-to-one coupling between Southern Ocean productivity and Antarctica climate. *Geophys. Res. Lett.* **49**, e2022GL098761 (2022).

24. Lambert, F., Bigler, M., Steffensen, J. P., Hutterli, M. & Fischer, H. Centennial mineral dust variability in high-resolution ice core data from Dome C, Antarctica. *Climate* **8**, 609–623 (2012).

25. McCave, I. N., Manighetti, B. & Robinson, S. G. Sortable silt and fine sediment size/composition slicing: parameters for palaeocurrent speed and palaeoceanography. *Paleoceanography* **10**, 593–610 (1995).

26. McCave, I. N., Thornalley, D. J. R. & Hall, I. R. Relation of sortable silt grain-size to deep-sea current speeds: Calibration of the 'Mud Current Meter'. *Deep Sea Res. Part I Oceanogr. Res. Pap.* **127**, 1–12 (2017).

27. McCave, I. N. & Andrews, J. T. Distinguishing current effects in sediments delivered to the ocean by ice. I. Principles, methods and examples. *Quat. Sci. Rev.* **212**, 92–107 (2019).

28. Wu, S. et al. Orbital-and millennial-scale Antarctic Circumpolar Current variability in Drake Passage over the past 140,000 years. *Nat. Commun.* **12**, 1–9 (2021).

29. Donohue, K., Tracey, K., Watts, D., Chidichimo, M. & Chereskin, T. Mean antarctic circumpolar current transport measured in Drake Passage. *Geophys. Res. Lett.* https://doi.org/10.1002/2016GL070319 (2016).

30. McCave, I. N., Crowhurst, S. J., Kuhn, G., Hillenbrand, C. D. & Meredith, M. P. Minimal change in Antarctic Circumpolar Current flow speed between the last glacial and Holocene. *Nat. Geosci.* **7**, 113–116 (2014).

31. Weber, M. E. et al. Millennial-scale variability in Antarctic ice-sheet discharge during the last deglaciation. *Nature* **510**, 134–138 (2014).

32. Meredith, M. P., Garabato, A. C. N., Gordon, A. L. & Johnson, G. C. Evolution of the deep and bottom waters of the Scotia Sea, Southern Ocean, during 1995-2005. *J. Clim.* **21**, 3327–3343 (2008).

33. Garcia, H. E. et al. Dissolved oxygen, apparent oxygen utilization, and oxygen saturation. *World Ocean Atlas 2013* **3**, 27 (2013).

34. Zweng, M. M. et al. Salinity. *World Ocean Atlas 2013* **2**, 39 (2013).

35. Toyos, M. H. et al. Antarctic circumpolar current dynamics at the Pacific entrance to the Drake Passage over the past 1.3 million years. *Paleoceanogr. Paleoclimatol.* **35**, e2019PA003773 (2020).

36. Huang, H., Gutjahr, M., Eisenhauer, A. & Kuhn, G. No detectable Weddell Sea Antarctic bottom water export during the last and penultimate glacial maximum. *Nat. Commun.* **11**, 1–10 (2020).

37. Menviel, L., Spence, P. & England, M. H. Contribution of enhanced Antarctic Bottom Water formation to Antarctic warm events and millennial-scale atmospheric CO_2 increase. *Earth Planet Sci. Lett.* **413**, 37–50 (2015).

38. Jaccard, S. L., Galbraith, E. D., Martínez-García, A. & Anderson, R. F. Covariation of deep Southern Ocean oxygenation and atmospheric CO_2 through the last ice age. *Nature* **530**, 207–210 (2016).

39. Gottschalk, J. et al. Southern Ocean link between changes in atmospheric CO_2 levels and northern-hemisphere climate anomalies during the last two glacial periods. *Quat. Sci. Rev.* **230**, 106067 (2020).

40. Skinner, L., Menviel, L., Broadfield, L., Gottschalk, J. & Greaves, M. Southern Ocean convection amplified past Antarctic warming and atmospheric CO_2 rise during Heinrich Stadial 4. *Commun. Earth Environ.* **1**, 1–8 (2020).

41. Gottschalk, J. et al. Abrupt changes in the southern extent of North Atlantic Deep Water during Dansgaard-Oeschger events. *Nat. Geosci.* **8**, 950–954 (2015).

42. Gottschalk, J. et al. Biological and physical controls in the Southern Ocean on past millennial-scale atmospheric CO_2 changes. *Nat. Commun.* **7**, 1–11 (2016).

43. Hayes, C. T. et al. A stagnation event in the deep South Atlantic during the last interglacial period. *Science* **346**, 1514–1517 (2014).

44. Parrenin, F. et al. Synchronous change of atmospheric CO_2 and Antarctic temperature during the last deglacial warming. *Science* **339**, 1060–1063 (2013).

45. Koenig, Z., Provost, C., Ferrari, R., Sennéchael, N. & Rio, M. H. Volume transport of the Antarctic Circumpolar Current:

Production and validation of a 20 year long time series obtained from in situ and satellite observations. *J. Geophys. Res. Oceans* **119**, 5407–5433 (2014).

46. Global Ocean Gridded L4 Sea Surface Heights And Derived Variables Reprocessed Copernicus Climate Service. E.U. Copernicus Marine Service Information (CMEMS). *Marine Data Store (MDS)*. https://doi.org/10.48670/moi-00145.

47. Lamy, F. et al. Five million years of Antarctic Circumpolar Current strength variability. *Nature* **627**, 789–796 (2024).

48. Ho, S. L. et al. Sea surface temperature variability in the Pacific sector of the Southern Ocean over the past 700 kyr. *Paleoceanography* **27**, PA4202 (2012).

49. Santos, T. P. et al. Prolonged warming of the Brazil Current precedes deglaciations. *Earth Planet Sc. Lett.* **463**, 1–12 (2017).

50. Roberts, J. et al. Deglacial changes in flow and frontal structure through the Drake Passage. *Earth Planet Sc. Lett.* **474**, 397–408 (2017).

51. Mazaud, A., Michel, E., Dewilde, F., & Turon, J. L. Variations of the Antarctic Circumpolar Current intensity during the past 500 ka. *Geochem. Geophys. Geosyst.* **11**, Q08007 (2010).

52. Starr, A. et al. Shifting Antarctic Circumpolar Current south of Africa over the past 1.9 million years. *Sci. Adv.* **11**, eadp1692 (2025).

53. Peeters, F. J. et al. Vigorous exchange between the Indian and Atlantic oceans at the end of the past five glacial periods. *Nature* **430**, 661–665 (2004).

54. Chadwick, M., Allen, C. S., Sime, L. C. & Hillenbrand, C. D. Analysing the timing of peak warming and minimum winter sea-ice extent in the Southern Ocean during MIS 5e. *Quat. Sci. Rev.* **229**, 106134 (2020).

55. Civel-Mazens, M. et al. Antarctic Polar Front migrations in the Kerguelen Plateau region, Southern Ocean, over the past 360 kyrs. *Glob. Planet. Change* **202**, 103526 (2021).

56. Bianchi, C. & Gersonde, R. The Southern Ocean surface between Marine Isotope Stages 6 and 5d: Shape and timing of climate changes. *Palaeogeogr. Palaeoclimatol. Palaeoecol.* **187**, 151–177 (2002).

57. Cortese, G. et al. Southwest Pacific Ocean response to a warmer world: insights from Marine Isotope Stage 5e. *Paleoceanography* **28**, 585–598 (2013).

58. Pichon, J. J. et al. Surface water temperature changes in the high latitudes of the Southern Hemisphere over the last glacial-interglacial cycle. *Paleoceanography* **7**, 289–318 (1992).

59. Fogwill, C. J. et al. Testing the sensitivity of the East Antarctic Ice Sheet to Southern Ocean dynamics: past changes and future implications. *J. Quat. Sci.* **29**, 91–98 (2014).

60. Spence, P. et al. Localized rapid warming of West Antarctic subsurface waters by remote winds. *Nat. Clim. Change* **7**, 595–603 (2017).

61. Turney, C. S. et al. Early Last Interglacial ocean warming drove substantial ice mass loss from Antarctica. *Proc. Natl Acad. Sci. USA* **117**, 3996–4006 (2020).

62. Milankovitch, M. K. Kanon der Erdbestrahlung und seine Anwendung auf das Eiszeitenproblem. *R. Serb. Acad. Spec. Publ.* **133**, 1–633 (1941).

63. Flores, J. A. & Sierro, F. J. Pronounced mid-Pleistocene southward shift of the Polar Front in the Atlantic sector of the Southern Ocean. *Deep-Sea Res. Pt. II* **54**, 2432–2442 (2007).

64. Berger, A. & Loutre, M. F. Insolation values for the climate of the last 10 million years. *Quat. Sci. Rev.* **10**, 297–317 (1991).

65. Schulz, M. & Mudelsee, M. REDFIT: estimating red-noise spectra directly from unevenly spaced paleoclimatic time series. *Comput. Geosci. UK* **28**, 421–426 (2002).

66. Li, M., Hinnov, L. & Kump, L. Acycle: Time-series analysis software for paleoclimate research and education. *Comput. Geosci. -UK* **127**, 12–22 (2019).

67. Torrence, C. & Compo, G. P. A practical guide to wavelet analysis. *Bull. Am. Meteorol. Soc.* **79**, 61–78 (1998).

68. Grinsted, A., Moore, J. C. & Jevrejeva, S. Application of the cross wavelet transform and wavelet coherence to geophysical time series. *Nonlinear Proc. Geoph.* **11**, 561–566 (2004).

69. Rutberg, R. L. & Broccoli, A. J. Response of the high-latitude southern hemisphere to precessional forcing: Implications for Pleistocene Ocean circulation. *Paleoceanogr. Paleoclimatol.* **34**, 1092–1106 (2019).

70. Persch, C. F., DiNezio, P. & Lovenduski, N. S. The impact of orbital precession on air-sea CO_2 exchange in the Southern Ocean. *Geophys. Res. Lett.* **50**, e2023GL103820 (2023).

71. Yun, K. S. et al. A transient coupled general circulation model (CGCM) simulation of the past 3 million years. *Climate* **19**, 1951–1974 (2023).

72. Jin, C. S. et al. Tectonic and orbital forcing of the South Asian monsoon in central Tibet during the late Oligocene. *Proc. Natl Acad. Sci. USA* **120**, e2214558120 (2023).

73. Lamy, F. et al. Precession modulation of the South Pacific westerly wind belt over the past million years. *Proc. Natl Acad. Sci. USA* **116**, 23455–23460 (2019).

74. Montade, V. et al. Teleconnection between the Intertropical Convergence Zone and southern westerly winds throughout the last deglaciation. *Geology* **43**, 735–738 (2015).

75. Ceppi, P., Hwang, Y. T., Liu, X., Frierson, D. M. & Hartmann, D. L. The relationship between the ITCZ and the Southern Hemispheric eddy-driven jet. *J. Geophys. Res. Atmos.* **118**, 5136–5146 (2013).

76. Saenko, O. A., Fyfe, J. C. & England, M. H. On the response of the oceanic wind-driven circulation to atmospheric CO_2 increase. *Clim. Dynam.* **25**, 415–426 (2005).

77. Lamy, F., Hebbeln, D. & Wefer, G. Late Quaternary precessional cycles of terrigenous sediment input off the Norte Chico, Chile (27.5°S) and palaeoclimatic implications. *Palaeogeogr. Palaeoclimatol. Palaeoecol.* **141**, 233–251 (1998).

78. Stuut, J. B. W. & Lamy, F. Climate variability at the southern boundaries of the Namib (southwestern Africa) and Atacama (northern Chile) coastal deserts during the last 120,000 yr. *Quat. Res.* **62**, 301–309 (2004).

79. Tachikawa, K., Timmermann, A., Vidal, L., Sonzogni, C. & Timm, O. E. CO_2 radiative forcing and Intertropical Convergence Zone influences on western Pacific warm pool climate over the past 400 ka. *Quat. Sci. Rev.* **86**, 24–34 (2014).

80. Yuan, X., Kaplan, M. R. & Cane, M. A. The interconnected global climate system—A review of tropical-polar teleconnections. *J. Clim.* **31**, 5765–5792 (2018).

81. Shevenell, A. E., Ingalls, A. E., Domack, E. W. & Kelly, C. Holocene Southern Ocean surface temperature variability west of the Antarctic Peninsula. *Nature* **470**, 250–254 (2011).

82. Markle, B. R. et al. Global atmospheric teleconnections during Dansgaard-Oeschger events. *Nat. Geosci.* **10**, 36–40 (2017).

83. Nair, A. et al. Southern Ocean sea ice and frontal changes during the Late Quaternary and their linkages to Asian summer monsoon. *Quat. Sci. Rev.* **213**, 93–104 (2019).

84. England, M. R., Polvani, L. M., Sun, L. & Deser, C. Tropical climate responses to projected Arctic and Antarctic sea-ice loss. *Nat. Geosci.* **13**, 275–281 (2020).

85. Burns, S. J. et al. Southern Hemisphere controls on ITCZ variability in southwest Madagascar over the past 117,000 years. *Quat. Sci. Rev.* **276**, 107317 (2022).

86. Herraiz-Borreguero, L. & Naveira Garabato, A. C. Poleward shift of circumpolar deep water threatens the East Antarctic Ice Sheet. *Nat. Clim. Change* **12**, 728–734 (2022).

87. Wilson, D. J. et al. Ice loss from the East Antarctic Ice Sheet during late Pleistocene interglacials. *Nature* **561**, 383–386 (2018).

88. Hillenbrand, C. D. et al. West Antarctic Ice Sheet retreat driven by Holocene warm water incursions. *Nature* **547**, 43–48 (2017).

89. Anderson, R. F. et al. Wind-driven upwelling in the Southern Ocean and the deglacial rise in atmospheric CO_2. *Science* **323**, 1443–1448 (2009).

90. Vandenbroucke, T. R. et al. Polar front shift and atmospheric CO_2 during the glacial maximum of the Early Paleozoic Icehouse. *Proc. Natl Acad. Sci. USA* **107**, 14983–14986 (2010).

91. Ai, X. E. et al. The southward migration of the Antarctic Circumpolar Current enhanced oceanic degassing of carbon dioxide during the last two deglaciations. *Commun. Earth Environ.* **5**, 58 (2024).

92. Menviel, L., Timmermann, A., Mouchet, A., & Timm, O. Climate and marine carbon cycle response to changes in the strength of the Southern Hemispheric westerlies. *Paleoceanography* **23**, PA4201 (2008).

93. d'Orgeville, M., Sijp, W. P., England, M. H., & Meissner, K. J. On the control of glacial-interglacial atmospheric CO_2 variations by the Southern Hemisphere westerlies. *Geophys. Res. Lett.* **37**, L21703 (2010).

94. Tschumi, T., Joos, F., & Parekh, P. How important are Southern Hemisphere wind changes for low glacial carbon dioxide? A model study. *Paleoceanography* **23**, PA4208 (2008).

95. Ai, X. E. et al. Southern Ocean upwelling, Earth's obliquity, and glacial-interglacial atmospheric CO_2 change. *Science* **370**, 1348–1352 (2020).

96. Köhler, P., Nehrbass-Ahles, C., Schmitt, J., Stocker, T. F. & Fischer, H. A 156 kyr smoothed history of the atmospheric greenhouse gases CO_2, CH_4, and N_2O and their radiative forcing. *Earth Syst. Sci. Data* **9**, 363–387 (2017).

97. Weber, M. E. et al. Dust transport from Patagonia to Antarctica—a new stratigraphic approach from the Scotia Sea and its implications for the last glacial cycle. *Quat. Sci. Rev.* **36**, 177–188 (2012).

98. Lu, L. et al. Supplementary Tables for the article "Extremely Poleward Shift of Antarctic Circumpolar Current by Eccentricity during the Last Interglacial" [Data set]. Zenodo. https://doi.org/10.5281/zenodo.14907902 (2025).

99. Lougheed, B. C. & Obrochta, S. P. A rapid, deterministic age-depth modeling routine for geological sequences with inherent depth uncertainty. *Paleoceanogr. Paleocl.* **34**, 122–133 (2019).

100. Bazin, L. et al. An optimized multi-proxy, multi-site Antarctic ice and gas orbital chronology (AICC2012): 120-800 ka. *Climate* **9**, 1715–1731 (2013).

101. Hammer, Ø., & Harper, D. A. Past: paleontological statistics software package for education and data analysis. *Palaeontol. electron.* **4**, 1–9 (2001).

102. Maldonado, A. et al. Contourite deposits in the central Scotia Sea: the importance of the Antarctic Circumpolar Current and the Weddell Gyre flows. *Palaeogeogr. Palaeoclimatol. Palaeoecol.* **198**, 187–221 (2003).

103. Garabato, A. C. N., Heywood, K. J. & Stevens, D. P. Modification and pathways of Southern Ocean deep waters in the Scotia Sea. *Deep Sea Res. Part I Oceanogr. Res. Pap.* **49**, 681–705 (2002).

104. Chaigneau, A., & Pizarro, O. Surface circulation and fronts of the South Pacific Ocean, east of 120 W. *Geophys. Res. Lett.* **32** (2005).

105. Orsi, A. H., Johnson, G. C. & Bullister, J. L. Circulation, mixing, and production of Antarctic Bottom Water. *Prog. Oceanogr.* **43**, 55–109 (1999).

106. Mulet, S. et al. The new CNES-CLS18 global mean dynamic topography. *Ocean Sci.* **17**, 789–808 (2021).

Author contributions

X.Z. designed the research. X.Z. and L.L. wrote, together with M.E.W., the manuscript. L.L. conducted the grain-size measurements. S.K., M.E.W., Z.C., V.P., B.T., T.C., W.Y., H.Y., X.G., S.Z.W., L.Z., S.M.W., Y.D., L.T., Q.Y., S.B., T.W., Y.M.M., Z.D., M.G., L.P., H.Y., B.H., and J.W. contributed to improving the manuscript. X.Z., L.L., S.K., M.E.W., Z.C., V.P., B.T., T.C., W.Y., H.Y., X.G., S.Z.W., L.Z., S.M.W., Y.D., L.T., Q.Y., S.B., T.W., Y.M.M., Z.D., M.G., L.P., H.Y., B.H., and J.W. contributed to the interpretation of the results and completed the manuscript.

Competing interests

The authors declare no competing interests.

Additional information

Supplementary information The online version contains supplementary material available at https://doi.org/10.1038/s41467-025-63933-x.

Correspondence and requests for materials should be addressed to Xufeng Zheng or Shuh-Ji Kao.

Peer review information *Nature Communications* thanks Pepijn Bakker, Natalia Vazquez Riveiros, and the other, anonymous, reviewer for their contribution to the peer review of this work. A peer review file is available.

Reprints and permissions information is available at http://www.nature.com/reprints

Publisher's note Springer Nature remains neutral with regard to jurisdictional claims in published maps and institutional affiliations.

[1]State Key Laboratory of Tropical Oceanography, South China Sea Institute of Oceanology, Chinese Academy of Sciences, Guangzhou, China. [2]State Key Laboratory of Marine Resource Utilization in the South China Sea, Hainan University, Haikou, China. [3]School of Atmospheric Sciences, Sun Yat-sen University, and Southern Marine Science and Engineering Guangdong Laboratory (Zhuhai), Zhuhai, China. [4]Guangdong Province Data Center of Terrestrial and Marine Ecosystems Carbon Cycle, Zhuhai, China. [5]Institute for Geosciences, Department of Geochemistry and Petrology, University of Bonn, Bonn, Germany. [6]British Antarctic Survey, Cambridge, UK. [7]Scripps Institution of Oceanography, University of California at San Diego, La Jolla, CA, USA. [8]Southern Marine Science and Engineering Guangdong Laboratory (Guangzhou), Guangzhou, China. [9]State Key Laboratory for Mineral Deposits Research, School of Earth Sciences and Engineering, Nanjing University, Nanjing, China. [10]State Key Laboratory of Loess Science, Institute of Earth Environment, Chinese Academy of Sciences, Xi'an, China. [11]State Key Laboratory of Physical Oceanography, Institute of Oceanographic Instrumentation, Shandong Academy of Sciences, Ji'nan, China. [12]Shandong Computer Science Center, Qilu University of Technology (Shandong Academy of Sciences), Ji'nan, China. [13]Institute of Earth Sciences, University of Lausanne, Lausanne, Switzerland. [14]State Key Laboratory of Deep-sea Science and Intelligence Technology, Institute of Deep-sea Science and Engineering, Chinese Academy of Sciences, Sanya, China. [15]Key Laboratory of Marine Geology and Environment, Institute of Oceanology, Chinese Academy of Sciences, Qingdao, China. [16]Earth and Environmental Studies, Montclair State University, Montclair, NJ, USA. [17]International Ocean Discovery Program, Texas A&M University, College Station, TX, USA. [18]NASA Goddard Space Flight Center, Planetary Magnetospheres Laboratory, Greenbelt, MD, USA. [19]Department of Astronomy, University of Maryland, College Park, MD, USA. [20]State Key Laboratory of Cryospheric Sciences, Chinese Academy of Sciences, Lanzhou, China. [21]Cadiz Oceanographic Centre. Spanish Institute of Oceanography (IEO), Spanish Research Council (CSIC), Cádiz, Spain. [22]Near Surface Land and Marine Geology, Geological Survey of Denmark and Greenland (GEUS), Aarhus University City 81, Aarhus C, Denmark. [23]Southern Marine Science and Engineering Guangdong Laboratory (Zhuhai), Zhuhai, China. [24]Department of Geography, Geology, Environment and Planning, Indiana University of Pennsylvania, Indiana, PA, USA. ✉e-mail: xufengzheng@hainanu.edu.cn; sjkao@hainanu.edu.cn